

**Performance assessment of photoelectrochemical CO₂ reduction
photocathode with patterned electrocatalysts: a multi-physical
model-based approach**

Yuzhu Chen^{1,2}, Chengxiang Xiang³, Meng Lin^{1,2,*}

¹ Department of Mechanical and Energy Engineering, Southern University of Science and Technology, Shenzhen 518055, China

² SUSTech Energy Institute for Carbon Neutrality, Southern University of Science and Technology, Shenzhen 518055, China

³ Liquid Sunlight Alliance, Department of Applied Physics and Material Science, California Institute of Technology, Pasadena, California 91125, United States

* Corresponding Author: linm@sustech.edu.cn

1. Methodology

To illustrate the behavior of a p-Si photocathode for CO₂ reduction at steady-state, a 2D numerical model was developed in this study. The model can be divided into three sub-models: *i)* optical model for predicting electron-hole generation rate, *ii)* semiconductor model for describing the transport of charge carriers in the semiconductor and the behavior of current transfer across the semiconductor-electrolyte/semiconductor-metal interfaces, and *iii)* CO₂R electrochemical model for describing mass transport, electrochemical and homogenous reaction kinetics for CO₂R.

1.1 Optical model

The electromagnetic wave (EMW) propagation was developed to provide a comprehensive model enabling future study on more complex structures. Three interfacial configurations were modelled in this study as shown in Figure S1. The EMW propagation was calculated in all components. Perpendicular AM1.5G front illumination (i.e., 0° incident angle) was defined as an input electromagnetic wave at the top boundary of electrolyte and the EMW wavelengths were varied from 280 to 1103 nm with $\Delta\lambda = 1$ nm, corresponding, respectively, to the smallest wavelength available from NREL ¹ and the bandgap of Si, E_g . The light was considered as transverse electric, and therefore, only the out-of-plane electric field was calculated. Bloch-Floquet theory was assumed for the periodicity on both sides of the computational domain and the boundary of emergent light was set at the bottom of p-Si photocathode. The various components were assumed rigid, homogeneous, and isotropic. The sub-model domains and its boundary conditions were indicated in Figure S1.

To account the optical effects in the electrolyte, a 1 μm thick layer of water in front of the p-Si photocathode was considered for minimizing computational time because the absorption loss by electrolyte was small (the water extinction coefficient (k) is below 3×10^{-6} in the wavelength range considered in the optical model). ^{2, 3} The thickness of the p-Si photocathode was 100 μm . The length of electrolyte and a p-Si photocathode

was 10 μm .

The location-dependent generation rate inside the p-Si photocathode can be calculated by solving Maxwell's curl equations for each frequency, ν ,

$$\nabla \times (\nabla \times \mathbf{E}(\mathbf{x}, \mathbf{y}, \nu)) - k_0^2 \tilde{n}(\nu)^2 \mathbf{E}(\mathbf{x}, \mathbf{y}, \nu) = 0 \quad (\text{Equation S1})$$

where $\mathbf{E}(\mathbf{x}, \mathbf{y}, \nu)$ is the local frequency-dependent electric vector field, $\tilde{n}(\nu) = n(\nu) - ik(\nu)$ is the complex refractive index, and k_0 is the free space wavenumber.

The optical power absorbed per unit volume was calculated by,

$$P_{\text{abs}}(\mathbf{x}, \mathbf{y}, \nu) = -\frac{1}{2} 2\pi\nu |\mathbf{E}(\mathbf{x}, \mathbf{y}, \nu)|^2 I\{\varepsilon(\mathbf{x}, \mathbf{y}, \nu)\} \quad (\text{Equation S2})$$

instead of calculating the divergence of the time-average Poynting vector, which is less robust in numerical computation. $I\{\varepsilon(\mathbf{x}, \mathbf{y}, \nu)\}$ is the imaginary part of the material's complex permittivity ($\varepsilon = \varepsilon_r \varepsilon_0 = (n + ik)^2 \varepsilon_0$, ε_0 is the vacuum permittivity). The location-dependent electron-hole generation rate, G , is the sum of all the individual frequencies,

$$G_n = G_p = G(\mathbf{x}, \mathbf{y}) = \int_{\infty}^{\nu_{\text{max}}} P_{\text{abs}}(\mathbf{x}, \mathbf{y}, \nu) / h \nu d\nu \quad (\text{Equation S3})$$

the upper integration boundary ν_{max} is $\nu_{\text{max}} \geq E_g/h$, and h is Planck's constant.

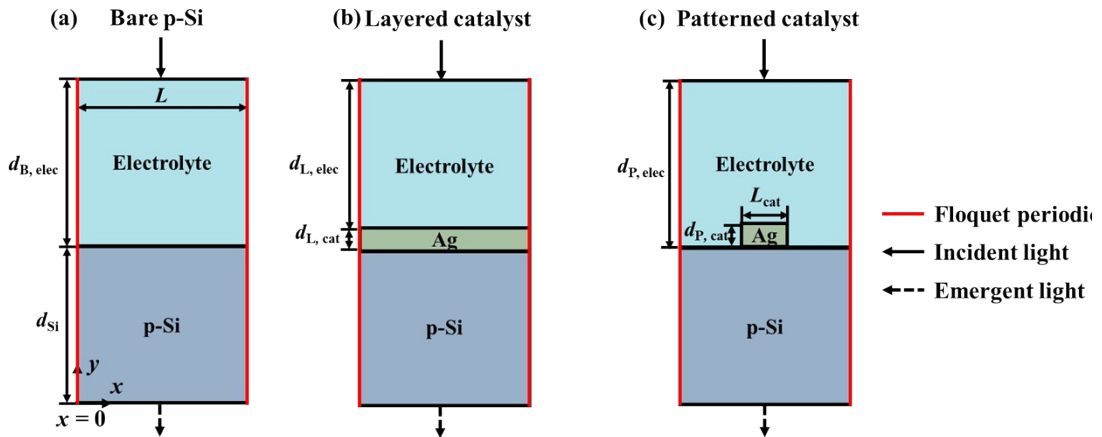


Figure S1 Scheme of computation domain of different modeling geometry and boundary conditions for the optical model. (a) Bare p-Si; (b) Layered catalyst; (c) Patterned catalyst. The boundary conditions of Floquet periodicity were marked with red lines. Boundaries of incident light (solid) and emergent light (dotted) were marked with arrows.

1.2 Semiconductor model

The simulation was performed to solve the potential and current transport in different

interfacial configurations of a p-Si photocathode, as depicted in Figure S2. The thickness and length of a p-Si photocathode were 100 μm and 10 μm , respectively. The length of semiconductor-electrolyte/metal interfaces was determined by the different coverage of metallic catalysts with the same size and the different sizes of metallic catalysts with the same coverage.

1.2.1 Charge transport

The static behavior of the electric field within the p-Si photocathode is related to the densities of charge carriers via the Poisson equation,

$$\nabla \cdot (\epsilon_0 \epsilon_{r,\text{Si}} \nabla \phi) = -\rho = q(n - p + N_{\text{a}}^- - N_{\text{d}}^+) \quad (\text{Equation S4})$$

Where $\epsilon_{r,\text{Si}}$ is the relative permittivity of silicon (see Table S3). n and p are the electron density and the hole density, respectively. N_{a}^- , and N_{d}^+ are ionized acceptor and ionized donor concentrations. q and ϕ are elementary charge and electrostatic potential. The electron and hole densities are given by the Maxwell-Boltzmann distribution for non-degenerated semiconductors,

$$n = N_{\text{C}} e^{-(E_{\text{c}} - E_{\text{F}})/k_{\text{B}}/T} \quad (\text{Equation S5})$$

$$p = N_{\text{V}} e^{-(E_{\text{F}} - E_{\text{v}})/k_{\text{B}}/T} \quad (\text{Equation S6})$$

where N_{C} and N_{V} are the effective density of states in the conduction band and valence band. E_{F} is the fermi level.

The steady-state charge conservation is given by,

$$\frac{1}{q} \nabla \cdot \mathbf{i}_{\text{n/p}} = U_{\text{n/p}} \quad (\text{Equation S7})$$

Where $U_{\text{n/p}}$ is the net electron or hole recombination rate and $\mathbf{i}_{\text{n/p}}$ is the electron or hole current density vectors due to the gradients of the local conduction band energy (∇E_{C}) and valence band energy (∇E_{V}), and the electron (∇n) and hole (∇p) concentration gradient, which is given by drift-diffusion equations,

$$\mathbf{i}_{\text{n}} = \mu_{\text{n}} n \nabla E_{\text{C}} + \mu_{\text{n}} k_{\text{B}} T \nabla n \quad (\text{Equation S8})$$

$$\mathbf{i}_{\text{p}} = \mu_{\text{p}} p \nabla E_{\text{V}} - \mu_{\text{p}} k_{\text{B}} T \nabla p \quad (\text{Equation S9})$$

Where $\mu_{n/p}$ is the electron or hole mobility, k_B is the Boltzmann constant, and T is the absolute temperature.

$U_{n/p}$ is composed of the carrier recombination ($R_{n/p}$) and electron-hole generation rate, which can be expressed as,

$$U_{n/p} \equiv R_{n/p}^{\text{SRH}} + R_{n/p}^{\text{rad}} + R_{n/p}^{\text{Au}} - G_{n/p} \quad (\text{Equation S10})$$

The location-dependent electron-hole generation rate ($G_{n/p}$) in the p-Si photocathode under illumination from the top of the electrolyte is obtained from the optical model, and shadowing or scattering events arising from the metallic sites on the p-Si photocathode surface are considered for the current calculations. Three types of recombination are considered in the bulk, *i.e.*, direct and Auger recombination and Shockley-Read-Hall. The direct recombination rate is given by,

$$R_n^{\text{dir}} = R_p^{\text{dir}} = C_{\text{dir}}(np - \gamma_n \gamma_p n_i^2) \quad (\text{Equation S11})$$

C_{dir} is the direct recombination factor of the p-Si photocathode (see Table S3). γ_n and γ_p are electron and hole degeneracy factors (equal to one for non-degenerated semiconductors). n_i is the intrinsic carrier concentration ($n_i = \sqrt{N_C N_V} \exp(-E_g/2k_B/T)$).

Auger recombination rate is given by,

$$R_n^{\text{Au}} = R_p^{\text{Au}} = (C_{\text{aug},n} n + C_{\text{aug},p} p)(np - \gamma_n \gamma_p n_i^2) \quad (\text{Equation S12})$$

where $C_{\text{aug},n}$ and $C_{\text{aug},p}$ are the Auger recombination factors for electrons and holes (see Table S1), respectively. The Shockley-Read-Hall recombination rate is given by,

$$R_n^{\text{SRH}} = R_p^{\text{SRH}} = \frac{np - \gamma_n \gamma_p n_i^2}{\tau_p(n + n_1) + \tau_n(p + p_1)} \quad (\text{Equation S13})$$

Where $\tau_{n/p}$ is the bulk electron or hole lifetimes, the electron and hole trap state densities are calculated by $n_1 = \gamma_n n_i e^{(E_t - E_i)/k_B/T}$ and $p_1 = \gamma_p n_i e^{-(E_t - E_i)/k_B/T}$ ($E_i = (E_C + E_V)/2 + k_B T/2$ is the fermi level for intrinsic semiconductors, and E_t is the trap energy level. $\Delta E_t = E_t - E_i$ is the difference between the trap energy level and the intrinsic Fermi level).

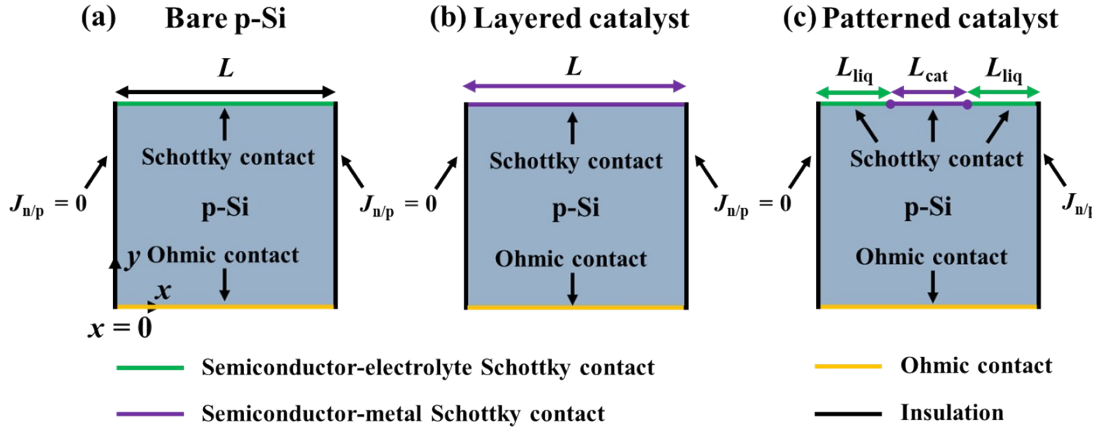


Figure S2 Scheme of computation domain of different modeling geometry and boundary conditions for the optical model. (a) Bare p-Si; (b) Layered catalyst; (c) Patterned catalyst. The boundaries of semiconductor-electrolyte Schottky contact are marked with green lines, and the boundaries of semiconductor-metal Schottky contact are marked with purple lines. The ohmic contact boundaries are marked with yellow lines, and insulation boundaries are marked with black lines.

1.2.2 Interfacial contact

Interfacial charge transfers at the semiconductor-metal and semiconductor-electrolyte interfaces are described by the Schottky contact mechanism,

$$i_n = -qv_{s,n}(n - n_0) \quad (\text{Equation S14})$$

$$i_p = qv_{s,p}(p - p_0) \quad (\text{Equation S15})$$

$$i_{sc} = (i_n + i_p) = i_l \quad (\text{Equation S16})$$

Where $v_{s,n}$ and $v_{s,p}$ are the electron and hole surface recombination velocities (see Table S3). $v_{s,p}$ was assumed to be zero because reduction reactions are of interest in this model, and the hole current is neglected. ⁴ i_{sc} is the total current density vector contributed by electron and hole current density (the total current densities at semiconductor-metal interface and semiconductor-electrolyte are labeled with $i_{sc,SM}$ and $i_{sc,SE}$, respectively). i_l is the electrolyte current density vector. n_0 and p_0 are the carrier concentrations under equilibrium given by,

$$n_0 = N_C e^{-\frac{\phi_b}{k_B T}} \quad (\text{Equation S17})$$

$$p_0 = N_V e^{-\frac{E_g - \phi_b}{k_B T}} \quad (\text{Equation S18})$$

Where ϕ_b is the barrier height determined by the fermi level of metallic electrocatalysts ($E_{F,Ag}$) at the semiconductor-metal Schottky contact and the Fermi level of electrolyte containing a redox couple ($E_{F,redox}$) at the semiconductor-electrolyte Schottky contact. The energy band diagram of semiconductor-metal Schottky contact under equilibrium is shown in Figure S3a. The barrier height $\phi_{b,SM}$ at the semiconductor-metal interface is the difference between p-Si work function and silver work function and can be determined by,

$$\phi_{b,SM} = E_{F,Ag} - E_{F,p-Si} \quad (\text{Equation S19})$$

Where ϕ_{Ag} and ϕ_{p-Si} are the work function of silver (Ag) and p-Si. ϕ_{Ag} was assumed to be 4.63 eV^{5,6} and ϕ_{p-Si} is calculated by,

$$E_v = E_{vac} - \chi - E_g \quad (\text{Equation S20})$$

$$E_{F,p-Si} = E_v + \zeta \quad (\text{Equation S21})$$

$$\zeta = k_B T \ln\left(\frac{N_v}{N_a}\right) \quad (\text{Equation S22})$$

Where E_c and E_v are the conduction band and valance band level, respectively. χ is the electron affinity energy of p-Si, E_{vac} is the vacuum energy level ($E_{vac} = 0$ eV as the usual convention), ζ is the distance of the valance band edge to the Fermi level of p-Si, and N_a is the doping concentration. The energy band diagram of semiconductor-electrolyte Schottky contact under equilibrium is shown in Figure S3b. The barrier height $\phi_{b,SE}$ at the semiconductor-electrolyte interface can be determined by,

$$\phi_{b,SE} = E_{F,redox} - E_{F,p-Si} \quad (\text{Equation S23})$$

$$E_{F,redox} = -4.44 \text{ eV} - eV_{fb,RHE} \quad (\text{Equation S24})$$

$$E_{F,p-Si} = \chi + E_g - \zeta - eV_{fb,RHE} - eV_H \quad (\text{Equation S25})$$

Where $V_{\text{fb,RHE}}$ is the flatband potential assumed to be 0.59 V vs. RHE. V_{H} is the potential drop in the Helmholtz layer. The applied potential (V_{a}) drops in the semiconductor space charge region (SCR) and the Helmholtz layer (HL),

$$V_{\text{a}} = \Delta\phi_{\text{sc}} + \Delta\phi_{\text{H}} \quad (\text{Equation S26})$$

where $\Delta\phi_{\text{sc}}$ and $\Delta\phi_{\text{H}}$ are the SCR and HL potential differences between no applied potential and applied potential. V_{a} is assumed to drop only into the SCR and V_{H} is assumed to be constant (see Table S3). The pH of the electrolyte is assumed to be 6.85, corresponding to the aqueous electrolyte saturated with CO_2 and 0.1 M KHCO_3 . Under bare p-Si and layered catalyst case, Schottky contacts are applied at the top interfaces of the p-Si photocathode. For the patterned catalyst case, two steps are used to calculate the photocurrent density: *i*) semiconductor-metal and semiconductor-electrolyte Schottky contact is applied at the top interfaces of p-Si photocathode to obtain the effective barrier height of semiconductor-metal ($\phi_{\text{b,SM}}^{\text{eff}}$) as the pinch-off occurs, *ii*) semiconductor-electrolyte interfaces are assumed to be passivated and no photocurrent flows through the interfaces in the patterned catalyst case. The obtained $\phi_{\text{b,SM}}^{\text{eff}}$ is used to calculate the photocurrent density at semiconductor-metal interfaces and serves as the current source term for the CO_2R electrochemical model.

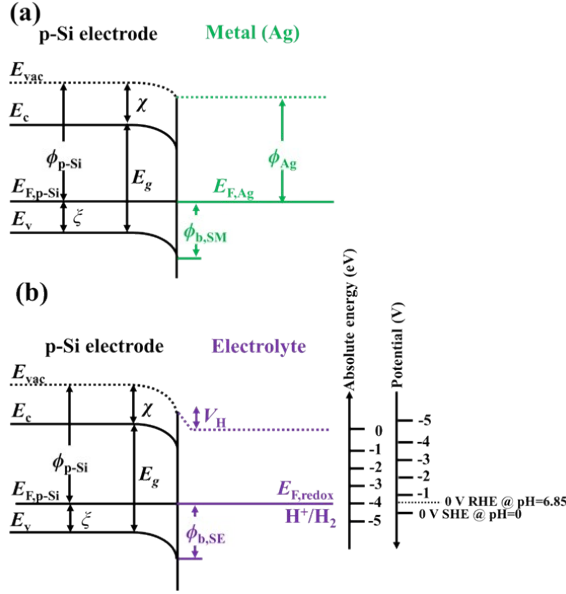


Figure S3. Schematic energy diagram of the semiconductor-metal (a) and semiconductor-electrolyte (b) contact in equilibrium.

1.2.3 Boundary conditions

The boundary conditions of the semiconductor model are shown in Figure S2. The ohmic contact is at the bottom of the p-Si photocathode marked with yellow lines, and Schottky contacts are at the top of the p-Si photocathode, semiconductor-electrolyte Schottky contacts are marked with green lines, and semiconductor-metal Schottky contacts are marked with purple lines. The insulation boundaries are on both sides of the p-Si photocathode marked with black lines. The bias (V_b) is applied at the ohmic contact.

1.3 CO₂R electrochemical model

Figure S4 shows a schematic of a 2D PEC model for CO₂R. The bulk electrolyte is 0.1 M KHCO₃ and the species in the CO₂ equilibrated electrolyte is dissolved CO₂, bicarbonate anions (HCO₃⁻), carbonate anions (CO₃²⁻), protons (H⁺), hydroxide anions (OH⁻), and potassium cations (K⁺). For simplicity, we neglected the effects on the CO₂ adsorption process caused by layered and patterned catalysts. We used a phenomenological Butler-Volmer based model with different kinetics parameters, i.e., exchange current densities and transfer number to distinguish the SC/E and SC/M interfaces. The current density at semiconductor-electrolyte interfaces is ignored in the

particulate catalyst case because the photocurrent is concentrated in the area covered by metallic catalysts. The local photocurrent density distribution of the layered catalyst case and the patterned catalyst case is shown in Figure S13.

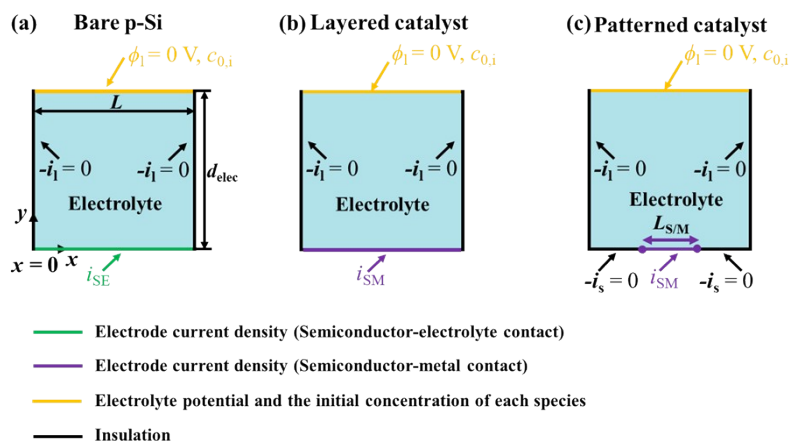
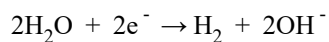
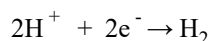
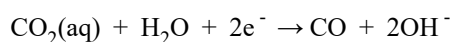
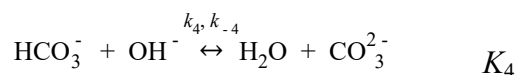
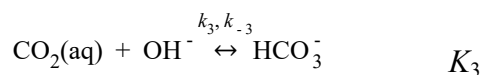
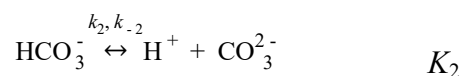
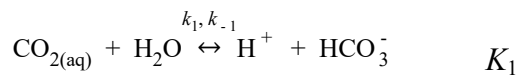


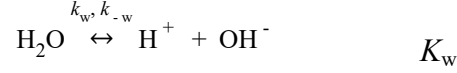
Figure S4. Schemes of computation domain and boundary conditions for the CO₂R electrochemical model. (a) Bare p-Si; (b) Layered catalyst; (c) Particulate catalyst. The electrolyte potential and initial concentration of each species are at the top of the electrolyte marked with yellow lines. The electrode current densities of the semiconductor-electrolyte and semiconductor-metal interface at the bottom of the electrolyte are marked with green and purple lines, respectively. The insulation boundaries are marked with black lines.

Three electrochemical reactions are considered in this model, which is assumed to be CO evolution reaction (COER) and H₂ evolution reaction (HER) in acidic and basic environments,



Five homogeneous reactions are considered in this model, including bicarbonate buffer and water dissociation reactions,





where k_n and k_{-n} are the rate constants for the forward and reverse directions of homogeneous reaction and K_n is the equilibrium constant.

2.3.1 Species transport in the electrolyte

The transport of species (CO_2 , HCO_3^- , CO_3^{2-} , H^+ , OH^- , K^+) in the electrolyte satisfy mass conservation,

$$\nabla \cdot N_i = R_{\text{ct},i} + R_{\text{b},i} \quad (\text{Equation S27})$$

Where N_i is the molar flux, $R_{\text{ct},i}$ is the volumetric reaction rate of charge transfer reactions, and $R_{\text{b},i}$ is the volumetric reaction rate of homogeneous reactions. $R_{\text{ct},i}$ can be calculated by,

$$R_{\text{ct},i} = - \sum_k \frac{v_{j,k} i_k}{n_k F} \quad (\text{Equation S28})$$

where n_k is the number of electrons transferred in charge transfer reaction k , i_k is the local current density at the electrode surface. $R_{\text{b},i}$ can be calculated by,

$$R_{\text{b},i} = \sum_n v_{j,n} (k_n \prod_{v_{j,n} < 0} c_j^{-v_{j,n}} - \frac{k_n}{K_n} \prod_{v_{j,n} > 0} c_j^{v_{j,n}}) \quad (\text{Equation S29})$$

where $v_{j,n}$ is the stoichiometric coefficient for species j in homogeneous reaction n .

The molar flux of species in the dilute electrolyte is described by the Nernst-Planck equation, which can be written as,

$$N_i = \underbrace{-D_i \nabla c_i}_{\text{diffusion}} - \underbrace{z_i \mu_i F c_i \nabla \phi_1}_{\text{migration}} \quad (\text{Equation S30})$$

Where D_i is the diffusion coefficient of species in the dilute electrolyte, μ_i is the ion mobility given by the Nernst-Einstein relationship ($\mu_i = \frac{D_i}{RT}$), ϕ_1 is the electrolyte potential, z_i is the charge number, and c_i is the concentration of species. Moreover, electroneutrality is needed to solve for the electrolyte ionic potential,

$$\sum_i z_i c_i = 0 \quad (\text{Equation S31})$$

2.3.2 Electron transport

Charge conservation and Ohm's law govern the solid-phase electric potential, ϕ_s , and current density, i_s ,

$$\nabla \cdot i_s = -\nabla \cdot i_l = -\sum_k i_k \quad (\text{Equation S32})$$

$$i_s = -\sigma \nabla \phi_s \quad (\text{Equation S33})$$

Where i_s and ϕ_s are the local current density at the electrode surface and electrode potential, respectively. i_l is the electrolyte current density and σ is the electronic conductivity of the electrode.

2.3.3 Charge-transfer kinetics and homogeneous bulk reactions

Charge-transfer kinetics at the cathode/electrolyte is modeled using Tafel kinetics for overpotentials greater than 0.2 V. The CO and H₂ current densities are calculated as,

$$i_{\text{CO}} = -i_{\text{o,COER}} \left(\frac{c_{\text{CO}_2(l)}}{c_{\text{CO}_2(l)}^{\text{ref}}} \right) \exp \left(-\frac{\alpha_{\text{c,COER}} F}{RT} \eta_{\text{COER}} \right) \quad (\text{Equation S34})$$

$$i_{\text{H}_2} = -i_{\text{o,HER}} \left(\frac{c_j}{c_j^{\text{ref}}} \right) \exp \left(-\frac{\alpha_{\text{c,HER}} F}{RT} \eta_{\text{HER}} \right) \quad (\text{Equation S35})$$

Where $i_{\text{o},k}$ is the exchange current density, α_{c} is the cathodic transfer coefficient, η_k is the kinetic overpotential, c_k is the local concentration at the electrode surface. Reference concentrations for both CO₂ ($c_{\text{CO}_2(l)}^{\text{ref}}$) and H⁺ ($c_{\text{H}^+}^{\text{ref}}$) are taken to be 1 M. Both acidic and alkaline HER can occur,

$$i_{\text{H}_2} = -i_{\text{o,HER}}^{\text{A}} \left(\frac{c_{\text{H}^+}}{c_{\text{H}^+}^{\text{ref}}} \right) \exp \left(-\frac{\alpha_{\text{c,HER}}^{\text{A}} F}{RT} \eta_{\text{HER}} \right) \quad \text{acidic} \quad (\text{Equation S36})$$

$$i_{\text{H}_2} = -i_{\text{o,HER}}^{\text{B}} \exp \left(-\frac{\alpha_{\text{c,HER}}^{\text{B}} F}{RT} \eta_{\text{HER}} \right) \quad \text{base} \quad (\text{Equation S37})$$

Where $i_{\text{o,HER}}^{\text{A}}$ and $i_{\text{o,HER}}^{\text{B}}$ are the exchange current density in acidic and base environment, respectively (see Table S3). $\alpha_{\text{c,HER}}^{\text{A}}$ and $\alpha_{\text{c,HER}}^{\text{B}}$ are cathodic transfer coefficients in the

acidic and base environment, respectively.

2.3.4 Polarization losses

The operating voltage for CO₂R is the sum of the equilibrium voltage and polarization losses. The polarization losses considered in this model include solution voltage loss, Nernstian loss, and kinetic overpotential for COER,

$$V_{ca} = V_{COER} + \eta_{Sol} \quad (\text{Equation S38})$$

where $V_{COER} = E_{0,COER} + \eta_{COER} N + \eta_{COER}$. $E_{0,COER}$ is the equilibrium potential of COER, η_{Sol} is the ohmic loss resulting from the resistance of the electrolyte ($\Delta\phi_{ohmic} =$

$\iint \frac{i_l}{\kappa} dx dy$, κ is the electrolyte conductivity, x and y are the positions) and the diffusion loss originating from the ionic gradient near the electrode ($\Delta\phi_{diffusion} =$

$\iint \sum_i \frac{Fz_i D_i \nabla c_i}{\kappa} dx dy$). $\eta_{COER} N$ is the loss due to the difference in pH at the cathode and

in the bulk electrolyte,

$$\eta_{N}^{COER} = \frac{2.303RT}{F} (\text{pH}_{ca} - \text{pH}_b) \quad (\text{Equation S39})$$

pH_{ca} and pH_b are the pH at the cathode and bulk electrolyte, respectively.

2.2.5 Boundary conditions

The boundary conditions of the CO₂R model are shown in Figure S4. The electrode current densities of semiconductor-electrolyte and semiconductor-metal interfaces obtained from the semiconductor model are at the bottom of the electrolyte marked with green and purple lines, respectively. The electrolyte potential and initial concentration of each species are set at the top of the electrolyte and marked with yellow lines. The initial concentration of each species (CO₂, HCO₃⁻, CO₃²⁻, H⁺, OH⁻, K⁺) was computed from the electroneutrality condition. The insulation boundaries are at both sides of the electrolyte marked with black lines. Additionally, the semiconductor-electrolyte interfaces at the bottom of the electrolyte were assumed to be insulation in the patterned catalyst case.

2.4 Operating point calculation

The operating point of the p-Si photocathode for CO₂R is given by solving the three sub-models in sequence. The equivalent circuit is shown in Figure S5. The behaviors of the p-Si photocathode include a current and voltage generating photodiode in series with an electrocatalytic element to drive the desired chemical reactions, a voltage loss for Nernstian loss, and a voltage loss for solution ohmic resistance. Additionally, HER and COER electrochemical reactions are considered in this model and can be described as parallel elements. The Nernstian loss is due to the difference in pH at the cathode and in the bulk electrolyte. The applied voltage (V_{app}) is expressed as,

$$V_{app} = V_{ca} + V_b \quad (\text{Equation S40})$$

The $V_{ca} = V_{COER} + \eta_{Sol}$. V_b is the bias set at the ohmic contact of the semiconductor model.

The flowchart of the coupled CO₂R photocathode model, including three submodels (optical, semiconductor, and CO₂R electrochemical models), depicts the simulation flow as shown in Figure S6. The optical model provides the generation rate, $G_{n/p}$, to the semiconductor model. The semiconductor model was coupled with the CO₂R electrochemical model via the constraint that $j_{ph} = j_{EC}$ (j_{EC} is the electrochemical current density for CO₂R). Thus, the semiconductor model provides the photocurrent density, j_{ph} , related to the mass source term, to the CO₂R electrochemical model. The electrochemical and species transport simulations were calculated using the CO₂R electrochemical model. Starting with an estimated operating electrochemical voltage (V_{EC}) of CO₂R under j_{EC} , the V_{EC} of each j_{EC} can be calculated through iteration until the V_{EC} converges ($|V_k EC - V_{k-1} EC| < 10^{-4}$). The operation points of the photocathode are decided by the operating photocurrent current, the V_{EC} , and the V_{app} .

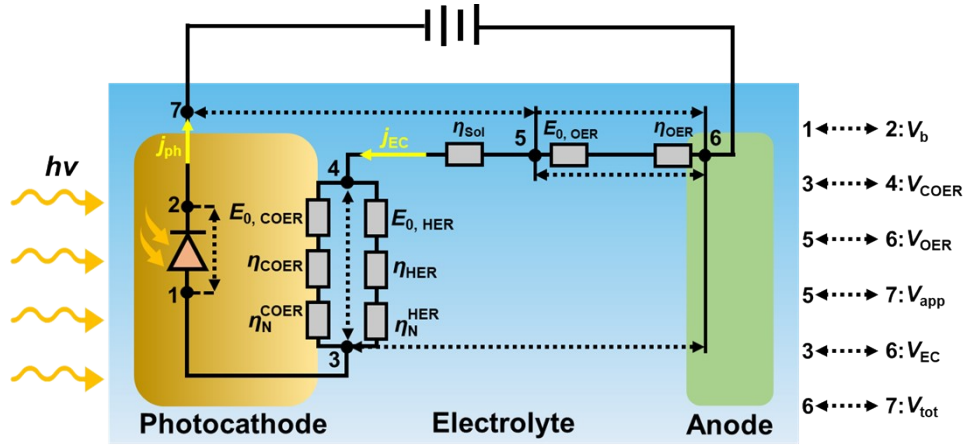


Figure S5. General schematic of a coupled photodiode-electrocatalyst device

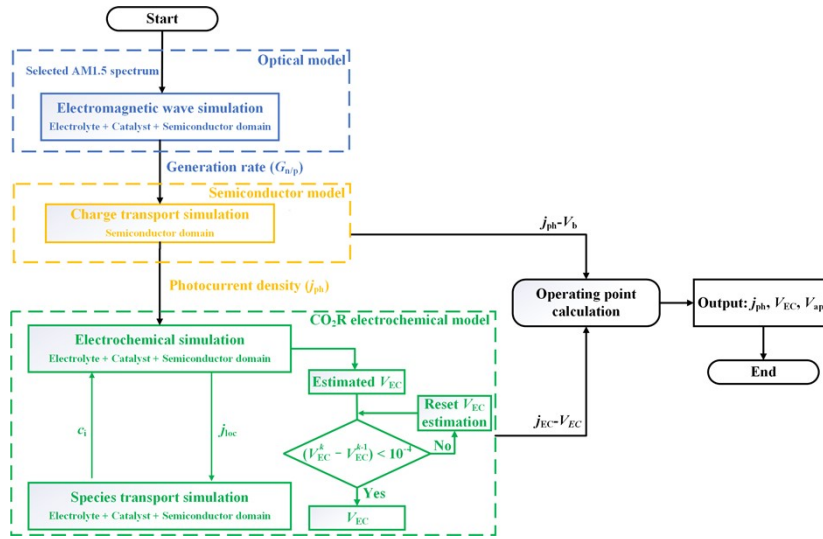


Figure S6. Flowchart of simulation process for the developed model.

2.5 Numerical details

The COMSOL Multiphysics 6.0 software solved all the governing equations using the MUMPS solver with a relative tolerance of 1×10^{-4} . The computing domains of the optical model were meshed using quadratic discretization orders and had a maximum element size of 50 nm, which ensured the calculation resolution was independent of the mesh element number. The variation of total generation rate in the p-Si photocathode was less than 1% as a further decrease of maximum element size. The computing domains of the semiconductor model and CO₂R electrochemical model were meshed with symmetric and linear mesh distributions and an element ratio of 1000. The symmetric distribution ensured a highly resolved mesh at each interface in the model. The variation of photocurrent density and potential at the interfaces in the p-Si was less

than 1% as a further increase in mesh number.

3. Model validation

i) Optical sub-model

In order to validate the optical model for predicting the optical properties, we compared the simulated reflectivity and absorption coefficient of p-Si photoabsorber, and the demonstrated experimental results available from literature⁷. The simulation was performed by EMW method. Perpendicular AM1.5G front illumination (i.e., 0° incident angle) was defined as an input electromagnetic wave and the EMW wavelengths were varied from 250 to 1200 nm with $\Delta\lambda = 1$ nm. The thickness of p-Si was assumed to 1 μm . As shown in Figure S7, the simulation results (marked in lines) were close agreement with experimentally observed trends (marked in circles).

ii) Semiconductor sub-model

In order to validate the semiconductor model for predicting the J - V curves under different interfacial configurations and pinch-off effects, we compared the simulated results and the demonstrated experimental results for Ni nanoparticles coated on an n-type Si surface in a solution with a reversible redox couple. The J - V curves of the three interfacial configurations were obtained through this model. The length and the thickness of the n-Si photoanode with a doping density of $7.9 \times 10^{14} \text{ cm}^{-3}$ were 2486 nm and 525 μm , respectively. The Schottky contacts were set at the top of the n-Si photoanode. The n-Si photoanode directly contacted the electrolyte in the n-Si/E case and the barrier height of n-Si/electrolyte interface was 0.84 eV. The n-Si photoanode directly contacted the Ni layer in the n-Si/Ni case and the barrier height of n-Si/Ni interface was 0.62 eV. The n-Si/electrolyte and n-Si/Ni interfaces were in the n-Si/Ni|E case. The length of the Ni dot was 174 nm and the coverage of the Ni dot was about 7 % in the n-Si/Ni|E case. The simulation solves the irradiation absorption and transport in the semiconductor by the Beer-Lambert law. The details of the experimental test were presented in literature⁸. The simulation results were marked in lines and the experimental data obtained were marked in circles (see Figure S8).

iii) CO₂R electrochemical sub-model

In order to validate the CO₂ electrochemical model, we compared the results of simulations and experimental data measured by Hatsukade et al.⁹ for planar electrodes to validate the developed CO₂ electrochemical model in this work (see Figure S9). The modeling parameters, such as geometry dimension, diffusion coefficient, exchange current density, transfer number, and equilibrium constant, were obtained from literature¹⁰. This comparison indicates that our model is valid, and the results are reasonable, which is in close agreement with experimentally observed trends.

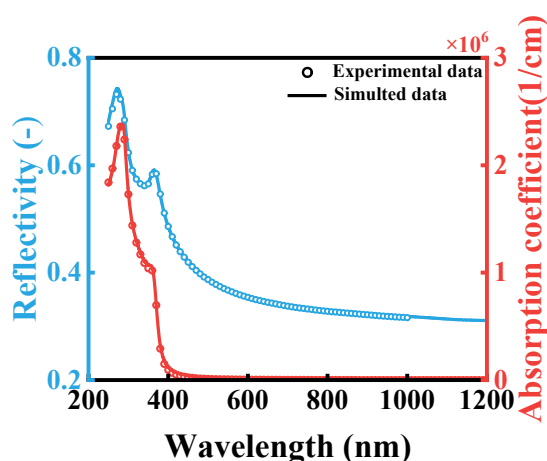


Figure S7. Reflectivity and absorption coefficient of p-Si photoabsorber as a function of wavelength.

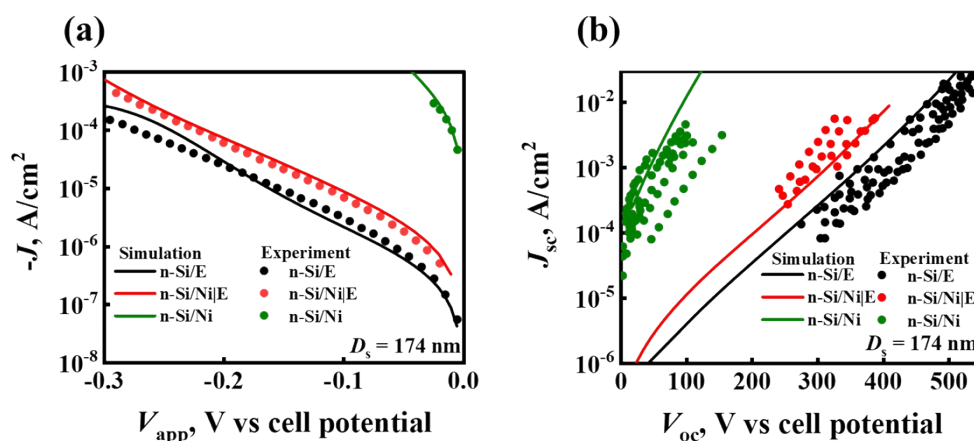


Figure S8. J - V curves of n-Si/Ni, n-Si/Ni|E, and n-Si/E electrodes in the dark (a) and illumination condition (Simulation results are marked in lines with different colors (black line: n-Si/Ni; red line: n-Si/Ni|E; green line: n-Si/E). Experimental data obtained from Rossi et al.⁸ are marked in circles with different colors (black dot: n-Si/Ni; red dot: n-Si/Ni|E;

green dot: n-Si/E).

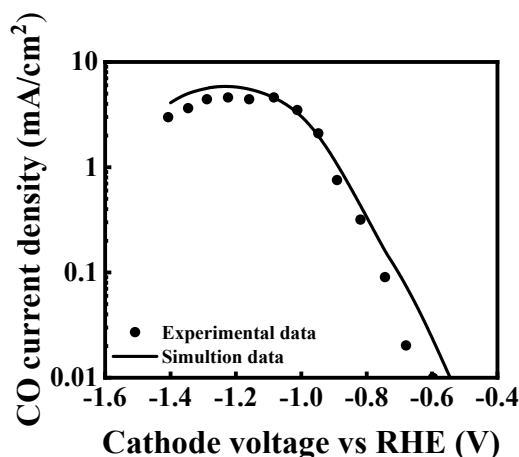


Figure S9. The simulated CO partial current density as a function of cathode voltage vs. RHE for the planar electrode compared to the experimental data measured by Hatsukade et al.⁹

iv) Influence of surface state and the catalytic activity of the metal

The kinetical parameters, i.e., exchange current density and the transfer number, of the catalyst on the photocathode surface under both dark and illumination conditions were considered to be identical, while the interfacial electronic states under both conditions were deemed to differ in this work.

The impacts of illumination conditions the kinetics of the catalyst in a PEC: Firstly, illumination can activate specific surface states on photoelectrode surfaces, which participate not only in the transient storage and transfer of electrons but also alter the electronic structure and chemical properties of active sites via light-induced surface adsorption or desorption reactions, thereby optimizing electrocatalytic performance. This mechanism enhances electron transport and reactions on the electrode surface.^{11, 12} Secondly, under illumination, a built-in electric field forms within the photoelectrode, promoting the effective separation of electron-hole pairs and reducing electron-hole pair recombination, thereby significantly boosting the charge supply needed for electrochemical reactions.¹³ To evaluate whether illumination conditions cause meaningful differences in the kinetics of the catalyst on the p-Si photocathode, we numerically simulated different kinetics at the semiconductor-metal interfaces to illustrate the possible effects of light conditions on the kinetic of the p-Si photocathode. For simplicity, we scaled up the exchange current density values in the reference case

of HER and COER reactions in Tafel equation by a factor of 1.2 and scaled down by a factor of 0.8, respectively, to simulate that the illumination conditions have a facilitating and a hindering effect on the kinetics of catalysts on the p-Si photocathode (see Figure S10a). The illumination showed limited impact of the kinetics of catalysts. For example, the variation of onset potential was lower than 0.001 V. Thus, the difference in kinetics of the catalyst on the photocathode surface under dark and illumination conditions can be neglected.

The interfacial electronic states under dark and illumination conditions were considered to be different in this work. Because interfacial states at the semiconductor surface can influence the barrier height of semiconductor-electrolyte interfaces under dark and illumination. This situation is possible due to different flatband potentials in the dark and under illumination. We assumed band edge pinning at the semiconductor-electrolyte interfaces and accounts for interface states in the p-Si photocathode surface which influenced the barrier height of semiconductor-electrolyte interfaces ($\phi_{b,SE}$) under dark and illumination. In the case of a V_a , the V_a drops in the SCR and the Helmholtz layer (see Equation S26). In this case, the change in $\Delta\phi_H$ remains constant and independent of the V_a . All the changes in V_a are within the $\Delta\phi_{sc}$ across SCR. To evaluate whether the influence of interface states in the p-Si photocathode of causes meaningful differences in the pinch-off effect and photocathode performance, we numerically simulated different the $\phi_{b,SE}$ case. We increased and decreased $\phi_{b,SE}$ by 0.1 eV from the reference case value to evaluate the impact on pinch-off effect due to the interfacial states. As shown in Figure S10b, the increase in the $\phi_{b,SE}$ caused a higher effective barrier height of the semiconductor-metal interfaces (ϕ_{mix}). These effects were taken into account in our model by varying the barrier heights at semiconductor-electrolyte and semiconductor-catalyst interfaces under dark and illumination conditions.

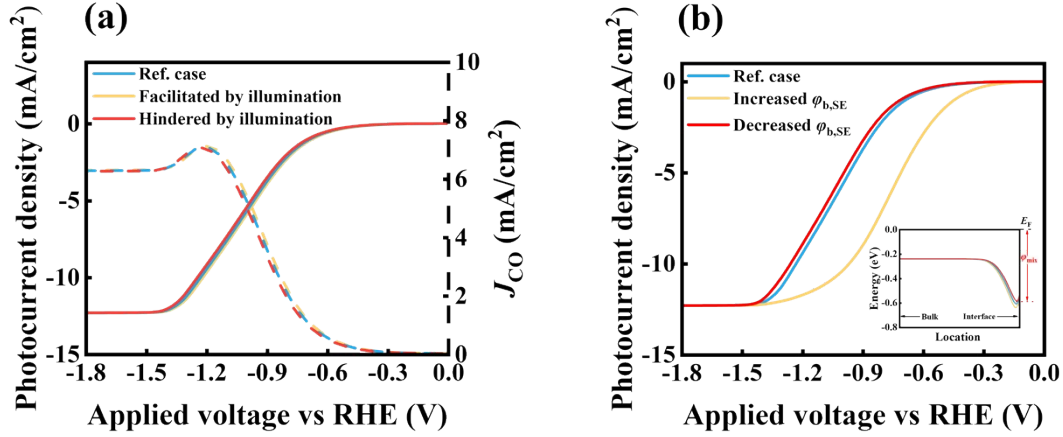


Figure S10. (a) the influence of illumination on the kinetics of the catalyst. Solid lines: J - V curves, dash lines: J_{CO} as a function of applied voltage; (b) the influence of interfacial states on the pinch-off effect and photocathode performance. Inset: the variation in effective barrier height with different barrier height of semiconductor-electrolyte interfaces.

v) Model validation for photoelectrochemical data

While, we have validated our model with existing literature. Here, to future show the validity of our model, we provide a comparison between the simulated results and the macroscopic voltammetry measured in the literature¹⁴ by Laskowski et al. (see Figure S11). The measured photoelectrochemical data for n-Si with a 5-s Ni deposition are consistent with that predicted by the model developed in this work. We used uniform islands of 60-nm radius covering 15% of the photoanode surface according to the literature. The exchange-current density and transfer number of the OER were obtained by fitting the Tafel equation (Equation S41) to experimental data,

$$j = j_{0,OER} \exp\left(\frac{\alpha_{OER} F \eta_{OER}}{RT}\right) \quad (\text{Equation S41})$$

where $j_{0,OER}$ is the exchange current density of OER, α_{OER} is the charge transfer coefficient of OER, F is Faraday constant, R is the gas constant, and T is the absolute temperature. Here, the values of $j_{0,OER}$ and α_{OER} were 5×10^{-5} A/m² and 0.8, respectively. The electron-hole generation rate was obtained by solving the EMW based optical model. We assumed high-barrier regions surrounding the pinched-off nanocontact (n-Si/Ni contact). The value of high barrier height was assumed to 0.91 eV and barrier height for n-Si/Ni contact was assumed to 0.61 eV.

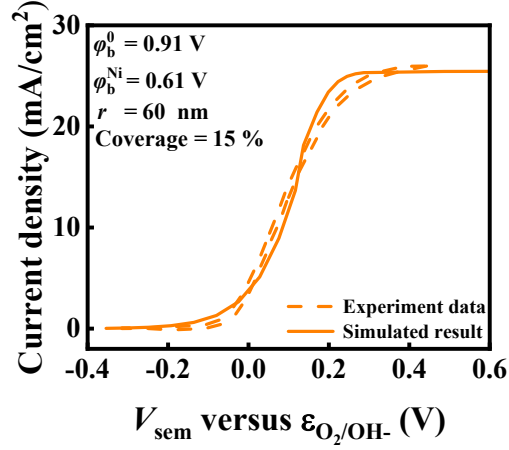


Figure S11. The comparison between the simulated results and the macroscopic voltammetry measured in the literature¹⁴. The solid line is the simulated result and dash lines are the experiment data.

4. Absorbance of electrolyte

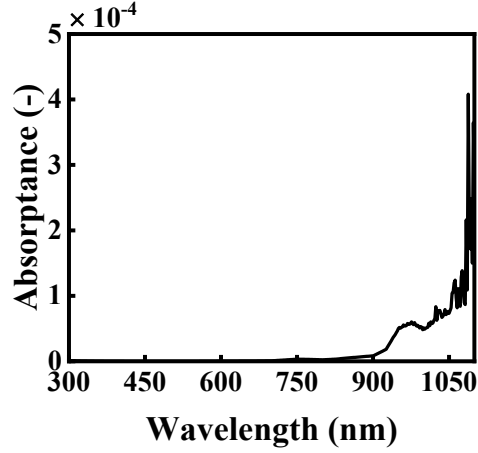


Figure S12. The water absorbance as a function of illumination wavelength for the bare p-Si case.

5. Energy breakdown

The total input energy (Q_{in}) of the photocathode of PEC for CO₂R can be expressed as

$$Q_{in} = Q_{solar} + Q_{app} \quad (\text{Equation S42})$$

Q_{solar} is the solar energy (AM1.5G) with a wavelength range varying from 280 to 1103 nm. Q_{app} is the electrical power provided by applied electrical power (Q_{app}) and can be expressed as,

$$Q_{app} = (Q_e) / \eta_{PV} \quad (\text{Equation S43})$$

The Q_e is the external electricity input ($Q_e = V_{EC} \times J_{ph} + |V_b| \times J_{ph}$). The $V_{EC} = V_{OER} - V_{COER} + \eta_{Sol}$. $V_{OER} = E_{o,OER} + \eta_{OER}$, and $V_{COER} = E_{o,CORE} - \eta_{COER} - \eta_N$. The $E_{o,OER}$ is 1.23

V vs. RHE, $E_{0, \text{CORE}}$ is -0.11 V vs. RHE, and η_{OER} is assumed as 0 V. The J_{ph} is the photocurrent density. For simplicity, we assumed the solar-to-electricity efficiency (η_{PV}) of photovoltaic (PV) as 20 %.

The optical losses include reflection loss and transmittance loss. The reflection energy is calculated by,

$$Q_{\text{Ref}} = |S11|^2 \times Q_{\text{solar}} \quad (\text{Equation S44})$$

Where $|S11|^2$ is the simulated reflection coefficient. The transmittance energy is calculated by,

$$Q_{\text{T}} = |S21|^2 \times Q_{\text{solar}} \quad (\text{Equation S45})$$

Where $|S21|^2$ is the simulated transmission coefficient.

The energy loss due to the electron-hole recombination loss and ohmic loss in the p-Si photocathode is calculated by,

$$Q_{\text{Sc}} = Q_{\text{solar}} - Q_{\text{Ref}} - Q_{\text{T}} + Q_{\text{e}} - Q_{\text{EC}} \quad (\text{Equation S46})$$

Where $Q_{\text{EC}} = Q_{\text{CO}} + Q_{\text{H}2} + Q_{\text{oph}} + Q_{\text{COER}} + Q_{\text{CO}2} + Q_{\text{HER}} + Q_{\text{sol}}$. The energy loss due to the solar to electricity conversion of PV is calculated by,

$$Q_{\text{PV}} = Q_{\text{app}} \times (1 - \eta_{\text{PV}}) \quad (\text{Equation S47})$$

The energy corresponding to the thermodynamics potential for driving COER (Q_{CO}) is calculated by,

$$Q_{\text{CO}} = (E_{0, \text{ORE}} - E_{0, \text{COER}}) \times J_{\text{CO}} \quad (\text{Equation S48})$$

Where the $E_{0, \text{COER}}$ is assumed as -0.11 V and $J_{\text{CO}} = J_{\text{ph}} \times \text{FE}_{\text{CO}}$ is the partial current density of COER. The energy corresponding to the thermodynamics potential for driving HER ($Q_{\text{H}2}$) is calculated by,

$$Q_{\text{H}2} = (E_{0, \text{ORE}} - E_{0, \text{HER}}) \times J_{\text{ph}} \times (1 - \text{FE}_{\text{CO}}) \quad (\text{Equation S49})$$

Where the $E_{0, \text{HER}}$ is assumed as 0 V and FE_{CO} is the CO Faradic efficiency. The energy losses due to the differences in pH (Q_{pH}) at the photocathode surface and in the bulk electrolyte are calculated by,

$$Q_{\text{pH}} = \Delta\phi_{\text{pH}} \times J_{\text{op}} = \frac{2.303RT}{F} (\text{pH}_{\text{ca}} - \text{pH}_{\text{b}}) \times J_{\text{ph}} \quad (\text{Equation S50})$$

The energy loss due to kinetic overpotential for COER (Q_{COER}) is calculated by,

$$Q_{\text{COER}} = \eta_{\text{COER}} \times J_{\text{CO}} - Q_{\text{CO}2} \quad (\text{Equation S51})$$

The energy loss due to the differences in concentration of CO₂ at the p-Si photocathode surface and in the bulk electrolyte (Q_{CO_2}) is calculated by,

$$Q_{CO_2} = \frac{RT}{nF} \ln \left(\frac{p_{CO_2,b}}{p_{CO_2,ca}} \right) \times J_{CO} \quad (\text{Equation S52})$$

Note that we isolated the CO₂ concentration effect from the concentration-dependent kinetic overpotential in the energy breakdown calculation to show the mass transfer effects better.

The energy loss due to kinetic overpotential for HER (Q_{HER}) is calculated by,

$$Q_{HER} = \eta_{HER} \times J_{ph} \times (1 - FE_{CO}) \quad (\text{Equation S53})$$

The energy loss due to solution voltage loss (Q_{Sol}) is calculated by,

$$Q_{Sol} = \eta_{Sol} \times J_{ph} \quad (\text{Equation S54})$$

where the η_{Sol} is the potential drop within the electrolyte.

The fraction of each energy component to the total solar energy input was defined as $f_i = Q_i / Q_{in}$.

Table S1. Eleven contributions to energy balance

Energy balance term	Expression
the energy loss from light reflection, f_{Ref}	$(S11 ^2 \times Q_{solar}) / (Q_{solar} + Q_{app})$
the energy loss from light transmission, f_T	$(S21 ^2 \times Q_{solar}) / (Q_{solar} + Q_{app})$
the energy loss from the electron-hole recombination loss and ohmic loss in the p-Si photocathode, f_{sc}	$(Q_{solar} - Q_{Ref} - Q_T + Q_e - Q_{EC}) / (Q_{solar} + Q_{app})$
the energy loss due to the solar to electricity conversion of PV, f_{PV}	$Q_{app} \times (1 - \eta_{PV}) / (Q_{solar} + Q_{app})$
the energy corresponding to the thermodynamics potential for driving COER, f_{CO}	$(E_{0,ORE} - E_{0,COER}) \times J_{CO} / (Q_{solar} + Q_{app})$
the energy corresponding to the thermodynamics potential for driving HER, f_{H2}	$(E_{0,ORE} - E_{0,HER}) \times J_{ph} \times (1 - FE_{CO}) / (Q_{solar} + Q_{app})$
the energy losses from the differences in pH at the photocathode surface and in the bulk electrolyte, f_{pH}	$2.303RT(pH_{ca} - pH_b) \times J_{ph} / F / (Q_{solar} + Q_{app})$
the energy loss due to the differences in concentration of CO ₂ at the p-Si photocathode surface and in the bulk electrolyte, Q_{CO_2}	$\frac{RT}{nF} \ln \left(\frac{p_{CO_2,b}}{p_{CO_2,ca}} \right) \times J_{CO} / (Q_{solar} + Q_{app})$
the energy loss from kinetic overpotential for COER, f_{COER}	$\eta_{COER} \times J_{CO} - \frac{RT}{nF} \ln \left(\frac{p_{CO_2,b}}{p_{CO_2,ca}} \right) \times J_{CO} / (Q_{solar} + Q_{app})$

the energy loss from kinetic overpotential
for HER, f_{HER}
the energy loss due to solution voltage
loss, f_{Sol}

$$\eta_{\text{HER}} \times J_{\text{ph}} \times (1 - \text{FE}_{\text{CO}}) / (Q_{\text{solar}} + Q_{\text{app}})$$

$$\eta_{\text{Sol}} \times J_{\text{ph}} / (Q_{\text{solar}} + Q_{\text{app}})$$

6. Photocurrent density at local sites

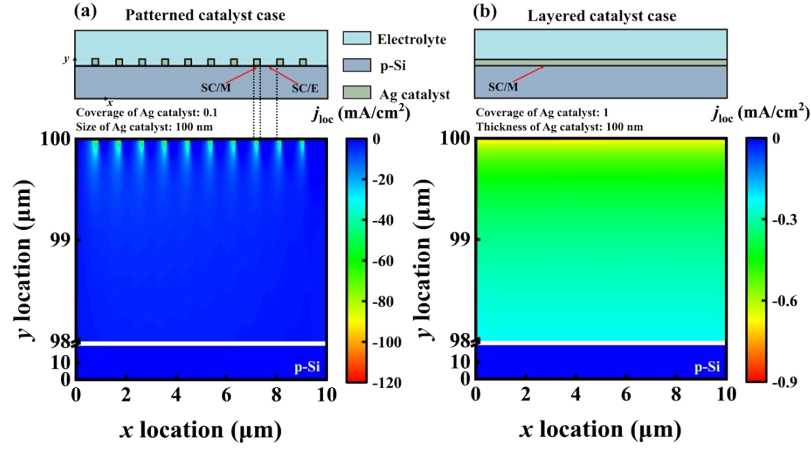


Figure S13. The photocurrent density distribution within the p-Si photoabsorber at -1.2 V. (a) the patterned catalyst case; (b) the layered catalyst case.

7. Explanation the different catalyst sizes on the saturation current density

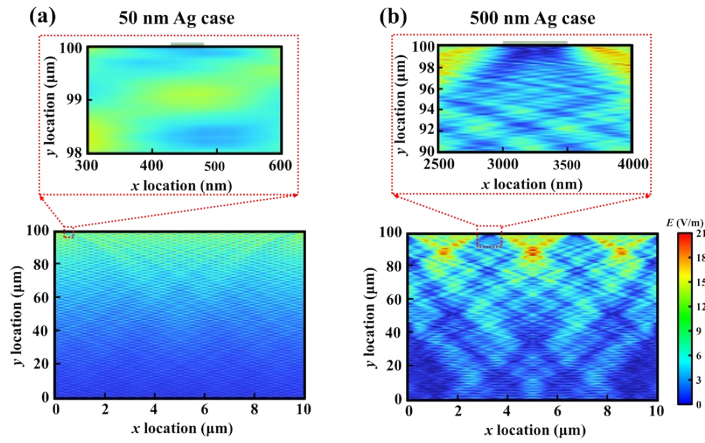


Figure S14. The electric field distribution within the p-Si photoabsorber. (a) the patterned scheme with 500 nm Ag; (b) the patterned scheme with 50 nm Ag.

8. The effect of catalyst's intrinsic activities on the photocathode performance

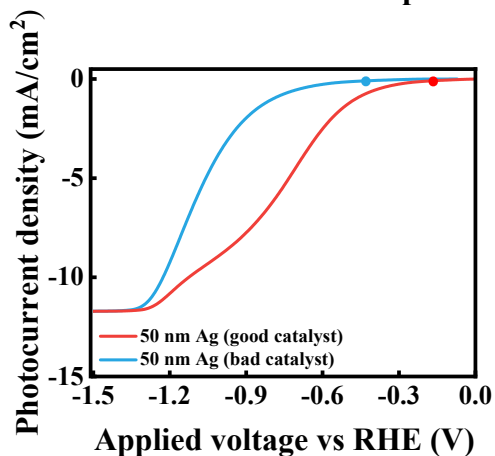


Figure S15. The J - V curves of patterned catalyst cases with different catalyst activity. The good catalyst condition is marked with a red line and the bad catalyst condition is marked with a blue line. The V_{on} is represented in circles.

9. The effect of catalyst sizes on the homogeneous reaction rate of CO₂

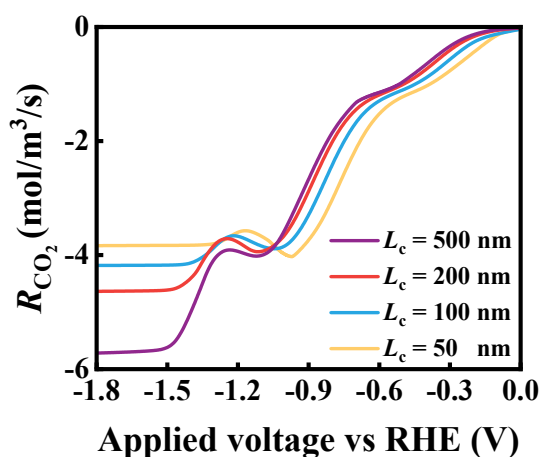


Figure S16. Homogeneous reaction rate of CO₂ as a function of V_{app} under different L_c . $L_c = 50$ nm is marked with a yellow line, $L_c = 100$ nm is marked with a blue line, $L_c = 200$ nm is marked with a red line, and $L_c = 500$ nm is marked with a purple line.

10. The effect of solar concentration ratios on the Faradic efficiency of CO

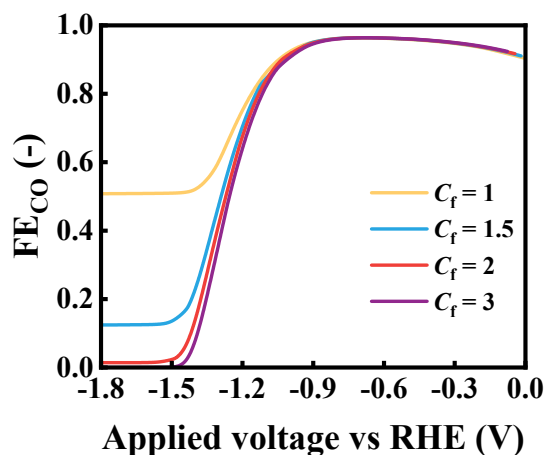


Figure S17. FE_{CO} as a function of V_{app} under different C_f . $C_f = 1$ is marked with a yellow line, $C_f = 1.5$ is marked with a blue line, $C_f = 2$ is marked with a red line, and $C_f = 3$ is marked with a purple line.

11. Performance of the patterned catalyst case under low light intensity

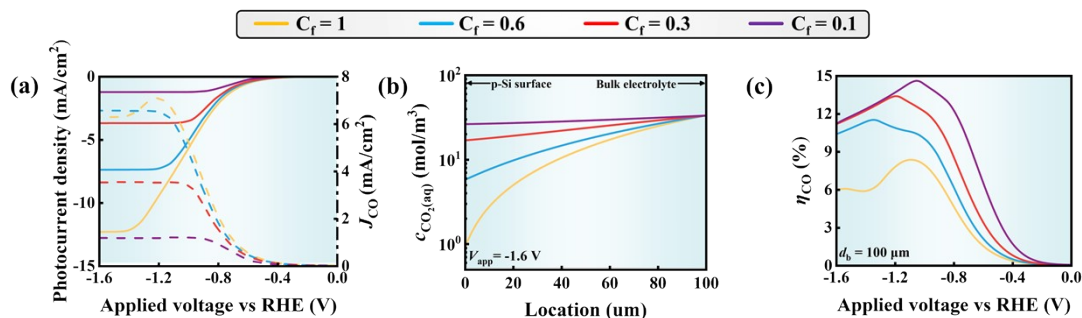


Figure S18. (a) J - V curves (solid lines) and J_{CO} (dash lines) as a function of V_{app} for the patterned case under different C_f . $C_f = 1$ (yellow line), $C_f = 0.6$ (blue line), $C_f = 0.3$ (red line), $C_f = 0.1$ (purple line); (b) c_{CO_2} as a function of location at -1.6 V under different C_f ; (c) The η_{CO} as a function of V_{app} under different C_f .

12. Mass transfer at gas-evolving electrodes

Electrolytically evolved bubbles enhance mass transfer to gas evolving electrodes because the growing and detaching of gas bubbles mix the electrolyte near the surface with electrolyte in the bulk.

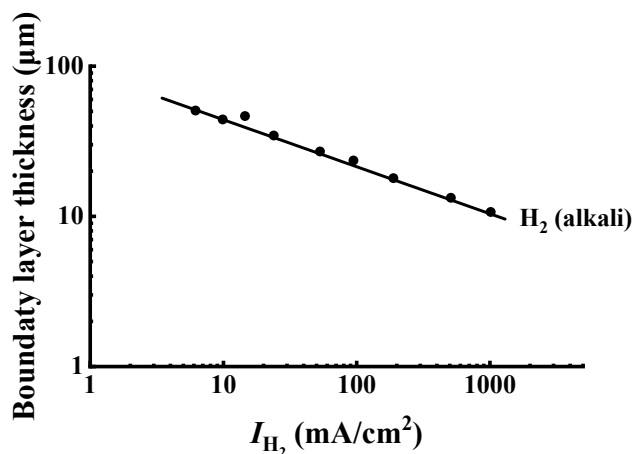


Figure S19 the boundary layer thickness as a function of current density for H₂ bubbles evolved in alkaline solution. The data is reproduced from literature¹⁵.

13. The effect of catalyst coverage on the valance bands

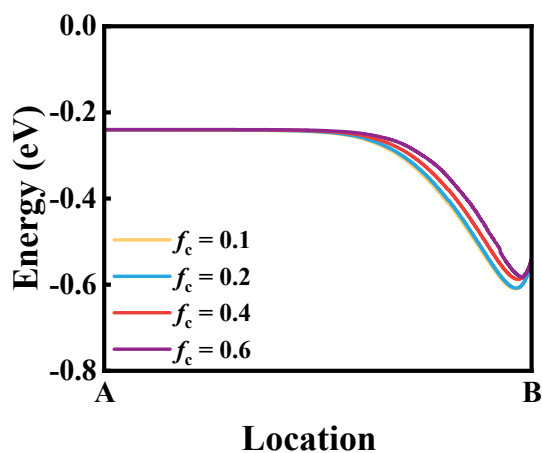


Figure S20. Scheme of the valance band edge under different catalyst coverage as a function of the location in bulk p-Si. $f_c = 0.1$ is marked with an yellow line, $f_c = 0.2$ is marked with a blue line, $f_c = 0.4$ is marked with a red line, and $f_c = 0.6$ is marked with a purple line.

14. The effect of catalyst coverage on the applied electrical power (Q_{app})

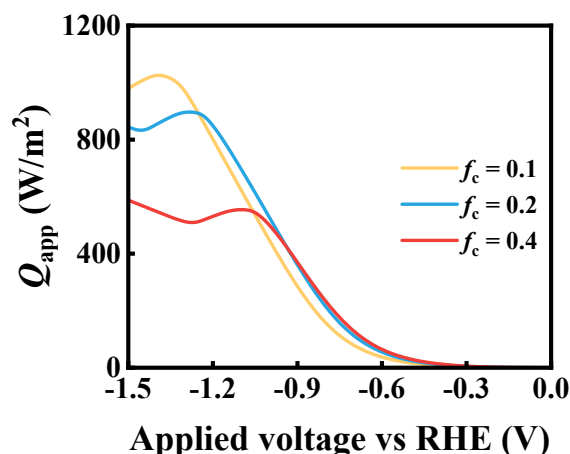


Figure S21. The Q_{app} as a function of V_{app} under different f_c . $f_c = 0.1$ is marked with a yellow line, $f_c = 0.2$ is marked with a blue line, and $f_c = 0.4$ is marked with a red line.

15. The performance of the patterned catalyst case under $d_b = 50$ um with different coverage of metal catalyst

A decrease in the d_b can increase the limiting current density of COER. In the case of $d_b = 50$ um, the absolute value of J_{sat} was 12.7 mA/cm^2 under $f_c = 0.05$ and that was close to the limiting current density of COER (12.1 mA/cm^2 under $f_c = 0.05$). The $f_c = 0.05$ was found to be the optimal value at low applied voltage ($V_{app} < -1.35$ V), leading to higher η_{CO} .

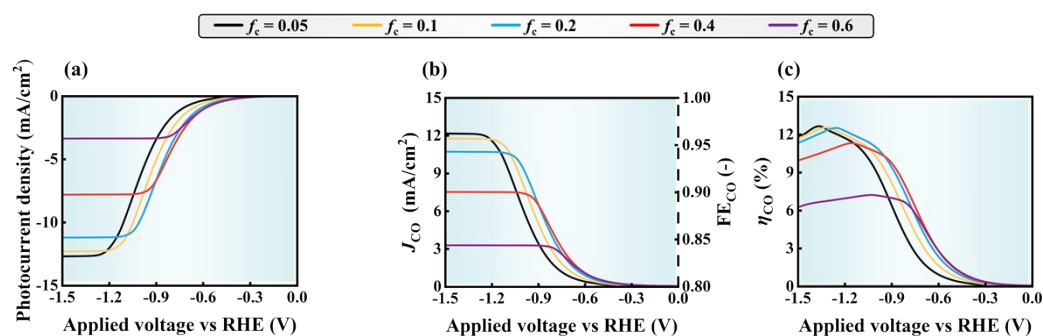


Figure S22. (a) J - V curves of the patterned catalyst case under $d_b = 50$ um with different f_c ; (b) the J_{CO} as a function of V_{app} under different f_c ; (c) The η_{CO} as a function of V_{app} under different f_c . $f_c = 0.05$ is marked with black line; $f_c = 0.1$ is marked with yellow line, $f_c = 0.2$ is marked with blue line, $f_c = 0.4$ is marked with red line, and $f_c = 0.6$ is marked with purple line.

Table S2. Geometry parameters of the reference cases

Parameter	Value	Unit
Length of the electrolyte, p-Si photocathode, and the layered catalyst, L	10	μm
The thickness of the electrolyte in the bare p-Si case (optical model), $d_{\text{B, elec}}$	1	μm
The thickness of the electrolyte in the layered catalyst case (optical model), $d_{\text{L, elec}}$	950	nm
The thickness of the catalysts in the layered catalyst case (optical model), $d_{\text{L, cat}}$	50	nm
Thickness of the electrolyte of the patterned catalyst case (optical model), $d_{\text{P, elec}}$	1	μm
The thickness of the catalysts in the patterned catalyst case (optical model), $d_{\text{P, cat}}$	50	nm
Thickness of the p-Si, d_{Si}	100	μm
Length of a patterned catalyst, $L_{\text{p, cat}}$	100	nm
The thickness of the electrolyte (CO ₂ R electrochemical model), d_{elec}	100	μm
Length of the semiconductor-metal interfaces (CO ₂ R electrochemical model), $L_{\text{S/M}}$	100	nm

Table S3. Physical parameters of the reference cases^{10, 16, 17}

Parameter	Value	Unit
Semiconductor model		
Band gap, E_{g}	1.12	eV
Electron affinity, χ	4.05	eV
Relative permittivity of silicon, $\epsilon_{\text{r, Si}}$	11.7	1
Density of states, conduction band, N_{c}	$\frac{T^{1.5}}{300} \times 2.80 \times 10^{19}$	cm^{-3}
Density of states, valence band, N_{v}	$\frac{T^{1.5}}{300} \times 1.04 \times 10^{19}$	cm^{-3}
Acceptor concentration, N_{a}	1×10^{15}	cm^{-3}
Electron mobility, μ_{n}	1450	$\text{cm}^2 \text{V}^{-1} \text{s}^{-1}$
Hole mobility, μ_{p}	500	$\text{cm}^2 \text{V}^{-1} \text{s}^{-1}$
Electron degeneracy factor, γ_{n}	1	1
Hole degeneracy factor, γ_{p}	1	1
Direct recombination factor, C_{dir}	0	$\text{cm}^3 \text{s}^{-1}$
Electron Shockley-Read-Hall lifetime, τ_{n}	10	us
Hole Shockley-Read-Hall lifetime, τ_{p}	10	us
Trap energy level, ΔE_{t}		
Auger recombination factor, electrons, $C_{\text{aug, n}}$	2.8×10^{-31}	$\text{cm}^6 \text{s}^{-1}$
Auger recombination factor, holes, $C_{\text{aug, p}}$	9.9×10^{-32}	$\text{cm}^6 \text{s}^{-1}$
Electron surface recombination velocity of semiconductor-metal interfaces, $v_{\text{s, n}}^{\text{S/M}}$	10	m s^{-1}
Electron surface recombination velocity of	0.01	m s^{-1}

semiconductor-electrolyte interfaces, $v_{s,n}^{S/E}$		
Work function of Ag, ϕ_{Ag}	4.63	eV
Potential drop in the Helmholtz layer, V_H	0.3	V
CO₂R electrochemical model		
D_{K^+}	1.957×10^{-5}	cm ² s ⁻¹
D_{H^+}	9.311×10^{-5}	cm ² s ⁻¹
D_{OH^-}	5.293×10^{-5}	cm ² s ⁻¹
$D_{HCO_3^-}$	1.185×10^{-5}	cm ² s ⁻¹
$D_{CO_3^{2-}}$	0.923×10^{-5}	cm ² s ⁻¹
D_{CO_2}	1.910×10^{-5}	cm ² s ⁻¹
K_1	$10^{-6.37}$	1
K_2	$10^{-10.32}$	mol L ⁻¹
K_3	K_1/K_w	L ² mol ⁻²
K_4	K_2/K_w	L mol ⁻¹
K_w	10^{-14}	mol ² L ⁻²
k_1	3.71×10^{-2}	s ⁻¹
k_2	59.44	s ⁻¹
k_3	2.23×10^3	L mol ⁻¹ s ⁻¹
k_4	6.0×10^9	L mol ⁻¹ s ⁻¹
k_w	2.4×10^{-5}	mol L ⁻¹ s ⁻¹
$E_{0,COER}$	-0.11	V
$E_{0,HER}$	0	V
$i_{0,COER}$	4.71×10^{-4}	mA cm ⁻²
$i_{o,HER}^A$	9.79×10^{-4}	mA cm ⁻²
$i_{o,HER}^B$	1.16×10^{-6}	mA cm ⁻²
$\alpha_{c,COER}$	0.44	1
$\alpha_{c,HER}^A$	0.27	1
$\alpha_{c,HER}^B$	0.36	1

Reference:

1. NREL, Reference Air Mass 1.5 Spectra, <https://www.nrel.gov/grid/solar-resource/spectra-am1.5.html>).
2. G. M. Hale and M. R. Querry, *Appl. Opt.*, 1973, **12**, 555-563.
3. H. Döscher, J. F. Geisz, T. G. Deutsch and J. A. Turner, *Energy Environ. Sci.*, 2014, **7**, 2951-2956.
4. P. Cendula, P. P. Sahoo, G. Cibira and P. J. T. J. o. P. C. C. Simon, 2019, **124**, 1269-1276.
5. A. M. Ismail, E. Csapó and C. Janáky, *Electrochimica Acta*, 2019, **313**, 171-178.
6. J. Rumble, *CRC Handbook of Chemistry and Physics*, CRC Press, 2016.
7. M. A. Green, *Solar Energy Materials and Solar Cells*, 2008, **92**, 1305-1310.
8. R. C. Rossi and N. Lewis, *Journal of Physical Chemistry B*, 2001, **105**, 12303-12318.
9. T. Hatsukade, K. P. Kuhl, E. R. Cave, D. N. Abram and T. F. Jaramillo, *Phys Chem Chem Phys*, 2014, **16**, 13814-13819.
10. L. C. Weng, A. T. Bell and A. Z. Weber, *Phys Chem Chem Phys*, 2018, **20**, 16973-16984.
11. J. E. Thorne, J.-W. Jang, E. Y. Liu and D. Wang, *Chemical science*, 2016, **7**, 3347-3354.
12. A. J. Bard, F.-R. F. Fan, A. S. Gioda, G. Nagasubramanian and H. S. J. F. D. o. t. C. S. White, 1980, **70**, 19-31.
13. C. Jiang, S. J. A. Moniz, A. Wang, T. Zhang and J. Tang, *Chem Soc Rev*, 2017, **46**, 4645-4660.
14. F. A. L. Laskowski, S. Z. Oener, M. R. Nellist, A. M. Gordon, D. C. Bain, J. L. Fehrs and S. W. Boettcher, *Nat Mater*, 2020, **19**, 69-76.
15. C. A. Sequeira, D. M. Santos, B. Šljukić and L. Amaral, *Brazilian Journal of Physics*, 2013, **43**, 199-208.
16. S. Kalogirou, *McEvoy's handbook of photovoltaics: fundamentals and applications*, Academic Press, 2017.
17. D. Bae, T. Pedersen, B. Seger, M. Malizia, A. Kuznetsov, O. Hansen, I. Chorkendorff and P. C. K. Vesborg, *Energy & Environmental Science*, 2015, **8**, 650-660.